

See discussions, stats, and author profiles for this publication at: <https://www.researchgate.net/publication/272170658>

Mechanisms of SnO₂ Nanoparticles Formation and Growth in Acid Ethanol Solution Derived from SAXS and Combined Raman-XAS Time-Resolved Studies

ARTICLE *in* CHEMISTRY OF MATERIALS · DECEMBER 2014

Impact Factor: 8.35 · DOI: 10.1021/cm5032688

CITATIONS

3

READS

101

6 AUTHORS, INCLUDING:



Florian Meneau

Centro Nacional de Pesquisa em Energia e Ma...

71 PUBLICATIONS 978 CITATIONS

SEE PROFILE



Celso V Santilli

São Paulo State University

237 PUBLICATIONS 2,983 CITATIONS

SEE PROFILE



S.H. Pulcinelli

São Paulo State University

185 PUBLICATIONS 2,415 CITATIONS

SEE PROFILE



Valerie Briois

French National Centre for Scientific Research

183 PUBLICATIONS 2,929 CITATIONS

SEE PROFILE

Mechanisms of SnO₂ Nanoparticles Formation and Growth in Acid Ethanol Solution Derived from SAXS and Combined Raman–XAS Time-Resolved Studies

Bruno L. Caetano,^{*,†,‡} Florian Meneau,^{*,‡,§} Celso V. Santilli,[†] Sandra H. Pulcinelli,[†] Marina Magnani,[†] and Valérie Briois[‡]

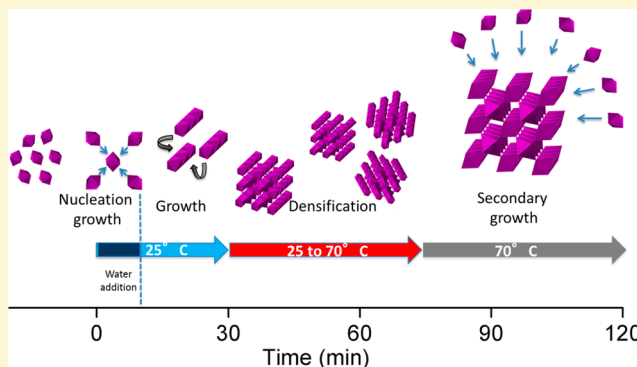
[†]Instituto de Química, UNESP, Rua Professor Francisco Degni, 55, 14800-900 Araraquara, São Paulo Brazil

[‡]Synchrotron SOLEIL, L'Orme des Merisiers, BP48, Saint Aubin, 91192 Gif-sur-Yvette, France

[§]Laboratório Nacional de Luz Síncrotron, CEP 13083-970, Caixa Postal 6192, Campinas, São Paulo, Brazil

Supporting Information

ABSTRACT: Although nanocrystalline SnO₂ is among the most intensely studied nanoscale semiconductor metal oxide, the actual mechanisms of nanoparticle formation and growth often remain unclear due to limited accessibility to in situ derived time-resolved information about the evolutions of precursor speciation and particle size. By overcoming such limitations, we report on the formation of SnO₂ nanoparticles by hydrolysis and condensation of precursors, and we give new insights on their nucleation and growth mechanisms based on in situ time-resolved SAXS and combined Raman/extended X-ray absorption fine structure (EXAFS) measurements. Raman and EXAFS spectroscopy indicate that the dissolution of tin tetrachloride pentahydrate in ethanol (precursor solution) leads to a mixture of tin chloride monomeric complexes [SnCl_x(H₂O)_{6-x}]^{4-x} composed of 41% [SnCl₅(H₂O)]⁻, 41% [SnCl₄(H₂O)₂], and 18% [SnCl₃(H₂O)₃]⁺. The combination of X-ray absorption spectroscopy (XAS) and Raman speciation with independent small-angle X-ray scattering (SAXS) results allows us to propose a five-step mechanism of formation. The first three steps are observed under water addition and aging at room temperature, corresponding to the prenucleation of low nuclearity species, followed by a monomer–tin-oxo cluster aggregation growth and cluster–cluster growth, leading to the formation of double or triple chains structure further interconnected to form SnO₂ nanoparticles. During heating from 25 to 70 °C and aging at 70 °C, a densification process followed by an advanced nanocrystallite growth through the addition of mononuclear species to the surface of the nanoparticles have been identified. These well-time separated steps could be used as a versatile way to control the growth processes and fine-tuning of the size of SnO₂ nanocrystallites.



1. INTRODUCTION

Nanocrystalline tin oxide coatings have emerged as future materials for various technological applications in daily life such as protection against corrosion,^{1,2} ultrafiltration membranes,³ gas sensors,⁴ catalysts,⁵ anodes for lithium rechargeable batteries,⁵ and transparent electrodes⁶ for smart windows, touch panel displays, voltage-dependent resistors, LED devices, and solar cells. For all of these applications, the performance of the device is greatly enhanced by the control of the size, morphology, and degree of aggregation of the nanoparticles. Among the different synthetic methods, the production of stable sols of crystalline tin oxide nanoparticles is of great interest for low-cost industrial applications. Indeed, the sol state can be easily used for dip- or spin-coatings, and the crystalline nature of the nanoparticles can reduce the postsynthesis thermal treatment step.⁷ One common route for preparing suspensions of monodisperse nanoparticles is so-called soft-

chemistry synthesis,⁸ which starts from molecular precursors in solution and gives rise to the nucleation and growth of solid networks after hydrolysis–condensation reactions.⁸

Almost all wet-chemistry methods used for the synthesis of tin oxide nanoparticles, like precipitation and sol–gel routes, are carried out in acidic and alkaline media, usually through the controlled hydrolysis of alkoxy,^{9,10} fluoro,¹¹ or chloro¹² precursors, followed in some cases by a solvothermal treatment to enhance the crystallinity.^{13,14} Although the results are dependent on temperature, solution composition, organic modification of precursor, and so on, several small polynuclear tin-oxo clusters were identified as crystalline products of controlled hydrolysis.^{8–12} The presence of several polynuclear

Received: September 4, 2014

Revised: October 31, 2014

Published: November 4, 2014

tin-oxo clusters of different nuclearity can play a role to the polymerization pathways because more highly condensed species might serve as molecular building blocks for the colloids and gels ultimately produced. Nevertheless, the participation of tin-oxo clusters as intermediate species in the mechanism of formation of SnO_2 nanocrystals has been overlooked in several studies, even those using advanced time-resolved techniques.^{14–16} This limited understanding of the mechanisms of precursor reactions leading to the nuclei formation and of subsequent growth hampers the tailoring of the size and shape of nanocrystalline SnO_2 particles in a predictable way.

In the classical LaMer theory of nucleation and growth, the particle formation from a homogeneous solution is described as a self-nucleation process. This happens through successive atom additions to preform nuclei and through dissolution of unstable phases with concomitant reprecipitation of stable phases.^{17,18} However, recent studies have found that nucleation of colloids could proceed by cluster–cluster aggregation rather than by individual cluster growth through the monomer accretion.^{19–22} This aggregative process leads to the formation of the so-called prenucleation cluster (PNC), with lower (or without) nucleation energy barrier.^{23,24} Indeed, because PNC is defined as small thermodynamically stable solutes, there is thus formally no phase boundary between the clusters and the surrounding solution, and thus their nucleation essentially occurs without supersaturation.²⁴ Moreover, PNC can have encoded structural motifs similar to the crystalline polymorph.²³ Such nonclassical mechanisms involving the presence of these PNC have been evidenced in numerous mineral systems.^{19–25} Other striking examples are the so-called magic-size nanoclusters, such as $(\text{CdSe})_{13}$, $(\text{CdSe})_{19}$, and $(\text{CdSe})_{33}$, which have been observed as intermediates preceding the nucleation of colloidal semiconductor nanocrystals.^{25–27}

Nucleation processes often occur on a relatively short time scale and thus are a challenge for direct time-resolved structural characterization of PNC. Thus, this feature makes the structural description of PNC poorly reliable for a full description of the mechanism and kinetics of nanoparticle nucleation and growth. Recently, the time resolution provided by Quick-X-ray absorption spectroscopy (XAS), wide-angle X-ray scattering (WAXS), and small-angle X-ray scattering (SAXS), available at a third-generation synchrotron radiation (SR) facility, combined with conventional Raman and UV–vis spectroscopies has emerged as a powerful and well-adapted approach for in situ reaction monitoring, allowing the characterization and specification of complex mixtures.^{28–33}

This paper deals with the in-depth time-resolved analysis of the initial stages of the formation of SnO_2 nanoparticles from the hydrolysis and condensation of $\text{SnCl}_4 \cdot 5\text{H}_2\text{O}$ dissolved in ethanol. Our methodology is based on a step-by-step approach with a tentative separation of the hydrolysis/nucleation and condensation/growth processes induced by room temperature (25 °C) controlled addition of water to the acid precursor ethanolic solution (pH = 0.7–1.5), followed by a heating step to 70 °C and subsequent isothermal aging. Because we are dealing at the beginning with transformation occurring in the first coordination shell around tin, simultaneous Sn K-edge extended X-ray absorption fine structure (EXAFS) and Raman time-resolved measurements were carried out for unravelling the local order around Sn, whereas time-resolved SAXS investigation was used to follow the evolution of number and size of nanoscopic polynuclear tin-oxo clusters. The analysis of

the tin speciation and of its dependence with the formation of PNC allowed for proposing consistent mechanisms for the formation of cassiterite (SnO_2) nanoparticles.

2. EXPERIMENTAL SECTION

2.1. SnO_2 Nanoparticles Synthesis. The precursor solution was prepared by dissolving tin tetrachloride pentahydrate ($\text{SnCl}_4 \cdot 5\text{H}_2\text{O}$) in absolute ethanol in order to achieve a Sn concentration of 0.2 mol/L and a pH = 0.9. The hydrolysis and condensation reactions were carried out under magnetic stirring by adding 7 mL of H_2O to 18 mL of the acid solution of precursors, followed by heating from RT to 70 °C. Irrespective of the used setup, the solution was vigorously stirred using a hot-plate magnetic stirrer device. The addition of water was carried out at RT using a peristaltic pump with a speed rate of 0.77 mL min^{-1} . The water addition took about 9 min and changed the molar hydrolysis ratio ($[\text{H}_2\text{O}]/[\text{Sn}]$) from 5 to 105. After complete water addition, the solution was aged at RT for 30 min before being heated to 70 °C with a heating ramp of 1 °C min^{-1} . Subsequently the solution was aged for 60 min at 70 °C. Supporting Information, Figure S1 shows the typical changes in hydrolysis ratios, temperature and pH characterizing the experimental steps monitored in situ by Raman/XAS and SAXS.

At the end of the reactions, the suspensions were cooled to RT, transferred inside acetylcellulose membrane bags (12–14,000 M_w), and submitted to static dialysis to eliminate chloride ions. The concentration of the remaining chloride ions at the end of dialysis was below the detection limit of the specific chloride electrode ($\approx 10^{-5}$ mol L^{-1}). The dialyzed suspension was centrifuged (14 000 rpm, 15 min) and isolated precipitates were dried at 60 °C during 24 h for further characterizations by XRD, HRTEM, and XAS.

2.2. Experimental Setups. The experimental setups used for XAS and SAXS characterizations are sketched in the Supporting Information, Figure S2a,b. Depending on the SR technique used for monitoring in situ the chemical and physical transformations, two different cells were used:

2.2.1. Quick-XAS. The solution was inserted into a temperature-controlled Kel-F liquid cell, equipped with X-ray transparent windows and with a thickness adjusted to an optical path of about 6 mm. This cell enables in situ combined Raman/XAFS measurements by using a Raman probe immersed into the solution, due to a special aperture at the top of the cell, as described in ref 29.

2.2.2. SAXS. The solution was pumped continuously from the reaction beaker to the X-ray quartz capillary cell (1.5 mm diameter, and wall thickness of 10 μm), where in situ SAXS measurements were carried out.³⁴ Both capillary cell and reaction vessel were temperature-controlled.

2.3. Combined Quick-XAS and Raman Spectroscopies. Time-resolved Quick-XAS and Raman data were collected simultaneously on the SAMBA beamline at the SOLEIL synchrotron.³⁵ The grazing incidence of the white and monochromatic X-ray beams on both Pd-coated collimating and focusing mirrors was set at 2.2 mrad, ensuring an efficient harmonic rejection around the Sn K edge (29 200 eV). The beam size at the sample position was of about 7×0.5 mm ($H \times V$). The time-resolved XAS data were collected in Quick-EXAFS mode,³⁶ and the monochromator was equipped with a Si(311) channel-cut operating at an oscillation frequency of 1 Hz, (corresponding to the acquisition of two spectra every second). XAS data were recorded in transmission mode using ionization chambers filled with Argon. Depending on the rate of the evolution of Sn-species in solution, spectra were averaged over 50 or 400 s to improve the signal-to-noise ratio.

Raman spectra were measured using a commercial RXN1 Raman spectrometer (from Kaiser Optical Systems, Inc.) equipped with a near-IR laser diode working at 785 nm, operating with a power output of 75 mW. A long-focal-length immersion optic with a working distance of 3 mm is in direct contact with the solution. Spectra were recorded between 100 and 3200 cm^{-1} in a continuous mode with a typical integration time of 13 s for each frame. The average resolution provided by the spectrometer is 2 cm^{-1} .

2.3.1. EXAFS Data Analysis. X-ray absorption data analysis was carried out using the Athena and Artemis software package.³⁷ Data were calibrated in energy using the maximum of the first derivative of a metallic tin foil recorded simultaneously with the samples data. For the EXAFS analysis, first a pre-edge background was removed using a linear function. A postedge background using the AUTOBK algorithm was applied with a cutoff $R_{\text{bkg}} = 1$ and k -weight = 2 in order to isolate the EXAFS oscillations $\chi(k)$. Then, the EXAFS data were Fourier transformed between 3.3 and 12.4 \AA^{-1} using a k^3 -weighting Kaiser-Bessel window with a $dk = 2$ apodization window. EXAFS fitting of distances, coordination numbers and Debye–Waller factors were performed with the Artemis interface to IFEFFIT³⁸ using least-squares refinements. The S_0^2 amplitude reduction parameter which takes into account multielectronic effects and the energy shift ΔE_0 were first calibrated by fitting relevant crystalline references as SnO_2 ³⁹ and $\text{SnCl}_2(\text{acac})_2$,⁴⁰ then both parameters were kept to fixed values for fitting the samples and equal to 1.11 and 29213.8 eV, respectively. The fitting procedure for the spectra recorded during RT reaction monitoring and leading to the structural parameters used in the text and figures is fully described in the Supporting Information.

2.3.2. Raman Normalization and Deconvolution. During the water addition, at the first stage of the reaction, the Raman intensities of all bands decrease due to dilution. In order to get rid of this effect, the intensity of the Raman bands were normalized in a consistent way, keeping constant the more intense band characteristic to the ethanol solvent located at 882 cm^{-1} . To evaluate components of complex band envelopes, the iterative least-squares curve-fitting available on the commercial GRAMS program (from Thermo scientific www.gramssuite.com/) was used. An exponential baseline was applied for modeling the background of the Raman spectra between 200 and 390 cm^{-1} . The spectra were then deconvoluted using Gaussian functions with full width half maximum (fwhm) values fixed at the mean values determined on a set of 60 Raman spectra collected during the first 30 min of reaction. The relative abundance of tin chloride $[\text{SnCl}_x(\text{H}_2\text{O})_{6-x}]^{4-x}$ complexes were estimated by calculating the areas under the peaks at approximately 320, 330, and 342 cm^{-1} which correspond to $x = 5, 4$ and 3 , respectively. An example of peak fitting procedure is displayed in Figure S3 (Supporting Information). The error bar in the determination of the species abundance by Raman is lower than 0.2%.

2.4. Small Angle X-ray Scattering. Time-resolved SAXS measurements were carried out on the SWING beamline at the SOLEIL synchrotron, in 8-bunches mode. The SAXS measurements were recorded using the AVIEX CCD camera (170×170 mm) placed in the vacuum detection tunnel. The sample to detector distance was set to 1.4 m and the energy to 7.7 keV. A 3 mm beamstop (vertical size) with a photodiode inserted in its center enabled to measure the transmitted intensity. The beam size at the sample position was about 50×300 μm ($V \times H$). The resulting q -range was 0.008–0.8 \AA^{-1} . The q -range calibration was done using silver behenate standard ($d_{\text{AgBe}} = 58.38$ \AA). SAXS data were acquired for 1 s with a period of 10 s for the first 30 min of reaction (water addition and aging at RT). The period was then set to 30 s for the rest of the experiment with the same exposure time.

The SAXS signal of the capillary filled with the solvent (a mixture of ethanol and water) was subtracted to the data, except for the first step of the reaction, where the water was added dropwise. In this latter case, a “dummy” SAXS experiment was performed with ethanol only, circulating in the capillary and water added dropwise in the same way as for the reaction (same capillary, X-ray beam position, and time-framing). A frame-by-frame subtraction was then done.

2.4.1. SAXS Data Analysis. Experimental SAXS curves were analyzed assuming a two-electron density model consisting of a dilute set of isolated particles or aggregates embedded in a homogeneous liquid solution. Under such assumptions, the scattered intensity $I(q)$ in the low- q region ($qR_g < 1$) can be approximated by the following relation:⁴¹

$$I(q) = I(0)e^{-(R_g^2 q^2)/3} \quad (1)$$

where R_g is the average radius of gyration of scatterers and $I(0)$ is the $\lim_{q \rightarrow 0} I(q)$, given by

$$I(0) = N \times (\rho_p - \rho_s)^2 \times V^2 \quad (2)$$

where N is the particle number density, ρ_p and ρ_s are the average electron densities of the particles and the solution, respectively, and V is the volume of the particle.

2.5. High-Resolution Transmission Electron Microscopy and X-ray Diffraction. For HRTEM studies, one drop of the solution containing the final SnO_2 nanoparticles redispersed in isopropyl alcohol was deposited onto lacey-carbon/copper grids. A JEOL JEM 3010 microscope operating at 300 kV (1.7 \AA resolution) was used. The XRD patterns were collected on a Bruker D2 Phaser with Ni filtered $\text{Cu K}\alpha$ radiation ($\lambda = 1.5406$ \AA) at a voltage of 30 kV and a current of 10 mA.

3. RESULTS

3.1. The Initial Tin Chloride Species. Figure 1 displays the RT characterizations of the acid ethanolic $\text{SnCl}_4 \cdot 5\text{H}_2\text{O}$

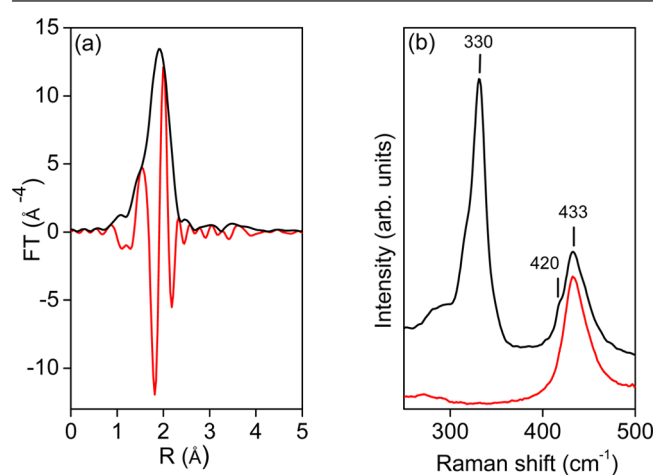


Figure 1. (a) Modulus and imaginary part of the FT of the EXAFS spectrum of the ethanolic $\text{SnCl}_4 \cdot 5\text{H}_2\text{O}$ solution before water addition and (b) Raman spectra of (red) ethanol and (black) ethanolic $\text{SnCl}_4 \cdot 5\text{H}_2\text{O}$ precursor solution.

solution before water addition carried out by EXAFS and Raman. As already reported in ref 12, the Fourier transform (FT) of the EXAFS spectrum presented in Figure 1a is characterized by an intense contribution centered around 2.0 \AA with a faintly marked shoulder around 1.5–1.6 \AA . This contribution is satisfactorily fitted, considering 4.6 ± 0.5 chlorine atoms at 2.38 ± 0.03 \AA and 1.4 ± 0.5 oxygen atoms at 2.11 ± 0.02 \AA from the tin absorbing atom. These distances are in good agreement with distances found in oxo halide–tin complexes.⁴² As the crystalline structure of $\text{SnCl}_4 \cdot 5\text{H}_2\text{O}$ is described as formed of $[\text{SnCl}_4(\text{H}_2\text{O})_2]$ molecular units,⁴³ the coordination number for chlorine atoms higher than 4, so-determined for ethanolic precursor solution, suggests that an excess of chlorine with respect to the chemical formula are present in the salt in the commercial product.

The comparison of the Raman spectrum of ethanol with one of the initial ethanolic $\text{SnCl}_4 \cdot 5\text{H}_2\text{O}$ solutions presented in Figure 1b displays an intense band in the 250–350 cm^{-1} Raman shift range, attributed to the Sn–Cl stretching mode. Actually, the characterization of tin chloride $[\text{SnCl}_x(\text{H}_2\text{O})_{6-x}]^{4-x}$ species in acetone solution by Taylor et al.⁴⁴ evidences a Raman red-shift for the Sn–Cl stretching mode with the increase of x : the main vibration is located at

308–312 cm^{-1} for $x = 6$, at 321 cm^{-1} for $x = 5$, at 330 cm^{-1} for $x = 4$ and at 342 cm^{-1} for $x = 3$. Herein, the Raman spectrum of $\text{SnCl}_4 \cdot 5\text{H}_2\text{O}$ dissolved in ethanol before water addition can be satisfactorily deconvoluted using Gaussian lines centered at 320, 330, and 342 cm^{-1} with respective fwhm values of 21.3, 12.8, and 20.8 cm^{-1} . This result is in good agreement with the presence of a mixture of tin chloride monomeric complexes with $x = 5, 4$, and 3 . According to the Placzek's relation,⁴⁵ which states that the area of a Raman line is proportional to the concentration of the scattering species in the irradiated volume, and assuming that Raman scattering cross-section for each Raman active tin chloride species is equivalent, the area of the deconvoluted lines in the 300–400 cm^{-1} range can be used for the determination of the relative contributions of the tin chloride complexes. Herein, we have found for the precursor acid solution the following mixture of monomeric $[\text{SnCl}_x(\text{H}_2\text{O})_{6-x}]^{4-x}$ species: 41% for $x = 5$, 41% for $x = 4$, and 18% for $x = 3$. It is noteworthy that this composition allows us to determine an average chlorine coordination $N_{\text{Cl}}(\text{Raman}) = (0.41 \times 5) + (0.41 \times 4) + (0.18 \times 3) = 4.2$. This value, deduced from Raman data, is in very good agreement with the EXAFS coordination number, $N_{\text{Cl}}(\text{EXAFS}) = 4.6 \pm 0.5$. Finally, it is noteworthy that the coordination of tin by oxygen atoms evidenced through the EXAFS results appears on the Raman spectrum of the precursor solution with the shoulder located at 420 cm^{-1} , structuring the broad line characterizing the vibration modes of ethanol solvent in the 400–470 cm^{-1} range. This line at 420 cm^{-1} is commonly observed for tin chloride hydrate species.⁴² Moreover, the lack of line centered around 351 cm^{-1} , as reported in the literature for the Raman spectrum of the dimeric species $[\text{Sn}_2\text{Cl}_6(\text{OH})_2(\text{H}_2\text{O})]_2 \cdot 4\text{H}_2\text{O}$,⁴⁴ suggests that only monomeric $[\text{SnCl}_x(\text{H}_2\text{O})_{6-x}]^{4-x}$ species are present in the precursor solution. The absence of oligomeric tin species in the initial solution was confirmed by the weak SAXS scattering intensity observed throughout the q region.

3.2. Effect of Water Addition and RT Aging.

3.2.1. Nanoscopic Features.

Figure 2 presents the 3D-SAXS

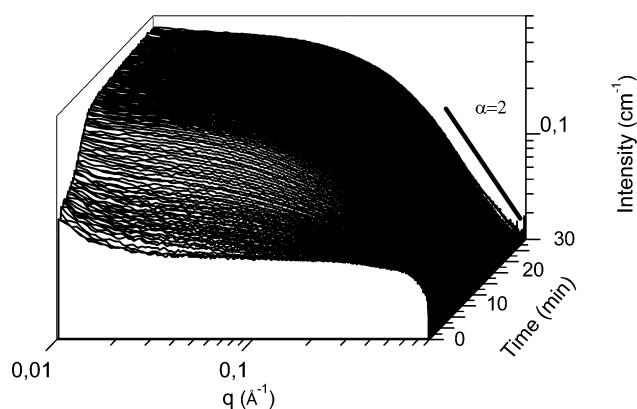


Figure 2. SAXS spectra as a function of time during the first 30 min of RT monitoring. The straight line displays the Porod decay with exponent $\alpha = 2$ observed at the end of the aging at RT.

spectra as a function of time, obtained during the first 30 min of reaction and corresponding to the water addition (10 min) and the subsequent aging at RT. We observe a strong increase of scattering intensity and a major change of shape of the scattering curves within the very first minutes of reaction.

At the beginning, the curves are characterized by a Gaussian decay in the high- q region and by a plateau at low q range. This

latter feature, also called Guinier region,⁴⁶ is characteristic of the scattering of a dilute set of noninteracting particles. This plateau shifts to lower q values as the reaction time advances, indicating that the individual nanoparticles increase in size. Moreover, during the aging at RT, an asymptotic linear trend (in the $\log I(q)$ versus $\log q$ plot), in the high- q range becomes evident, which satisfies the Porod law $I(q) \sim q^{-\alpha}$. For a biphasic system with a (sharp and smooth) interface of dimensionality D , the Porod exponent is given by $\alpha = 2d - D$, where d is the dimensionality of the scattering object (e.g., 3 for spherical particles ($\alpha = 4$), 2 for a plate-like particles ($\alpha = 2$), and 1 for rod-like particles ($\alpha = 1$)). The experimental value of the Porod exponent increases from 1.7 to 2.0 during the RT aging, indicating the presence of nonspherical particles. The experimental Porod exponent of $\alpha = 2$ could correspond to a plate-like morphology or to the association of a polydisperse mixture of globular nanoparticles and of small linear chains (oligomers).⁴⁶

Figure 3 shows the time evolution of R_g and $I(0)$ as a function of time. The average Guinier radii strongly increase

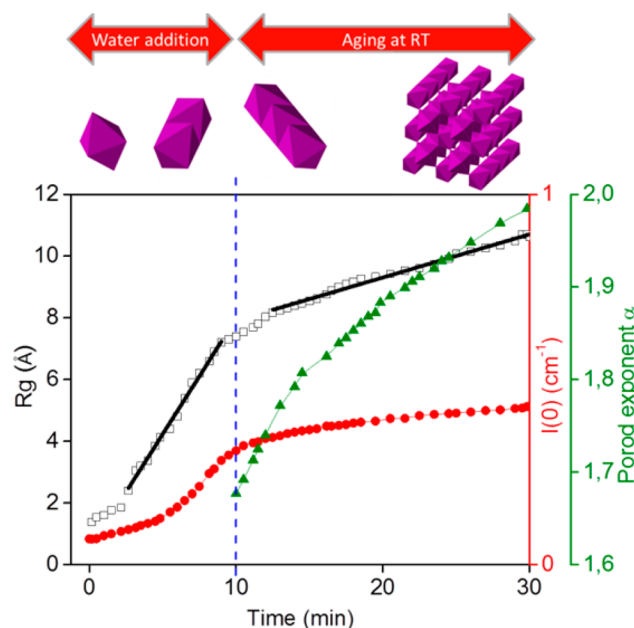


Figure 3. Time evolution of the (black \square) Guinier radius, (red \bullet) $I(0)$, and (green \blacktriangle) the Porod exponent obtained from the analysis of the SAXS experimental data with eqs 1 and 2. The schematics illustrate the monomers, dimers, and oligomeric species having R_g values consistent with the evolution of solution scattering patterns during the first 30 min of RT reaction.

from 1.4 to 8 Å within the first 10 min corresponding to water addition, to further increase linearly, but at a rate about 5 times slower, during the next 20 min of RT aging, to reach a final value of 10.7 Å. The initial R_g values correspond to the monomers and the formation of the first dimers and then to the formation of oligomeric species with increasing nuclearity. Indeed, Li et al.⁴⁷ have given the relationship between the maximum distance to encompass a polyhedron into a sphere, and thus to R_g . For an isolated monomer, with a long Sn–Cl distance of 2.38 Å, we obtain a R_g of 1.9 Å. Considering linear arrangements of edge sharing octahedra, we obtain $R_g = 2.6$ Å for a dimer, 3.9, 5.2, and 6.5 Å for a trimer, tetramer, and pentamer, respectively. For higher R_g values, tridimensional tin

oxo clusters can be described by the cassiterite structure as shown in Figure 3.

The correlation between these idealized structures and the time evolution of the average R_g values is schematized in Figure 3. The evolution of the equilibria between these different species, leading to the growth of denser polycondensed clusters, is consistent with the increase of the slope of the Porod tail. Moreover, the time dependency of the average radii of gyration (Figure 3) is described by two straight segments: one corresponding to the initial period of water addition and the other one to the RT aging period. These two linear growth regimes, $R_g - R_{g0} = kt$, with two distinct kinetic rates k , indicate a behavior consistent with the reaction-limited growth kinetics²⁵ controlled by two different mechanisms. Information about the nature of the tin species participating to these reaction-limited growth processes is presented in the following section.

3.2.2. Evolution of Tin Species. Figure 4 displays the evolution of the FTs of the EXAFS signals and of Raman

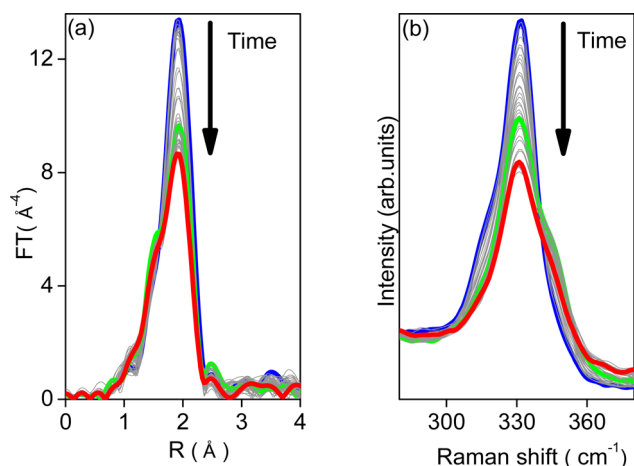


Figure 4. Time evolution of (a) the FT moduli of the EXAFS signals and (b) the Raman spectra during the first 30 min of RT reaction; (blue lines) spectra recorded before water addition, (green lines) spectra after completion of water addition, and (red lines) spectra recorded at the end of RT aging.

spectra as a function of time, measured during the first 30 min of reaction. Both data sets are consistent with the exchange of chlorine ligands by water molecules upon the first 10 min of water addition. On one hand, the FTs evidence a clear decrease of the main peak located at 2 Å, whereas the intensity of the shoulder at ≈ 1.5 – 1.6 Å is maintained. On the other hand, the total area of the broad Raman band characteristic of the overlap of Sn–Cl stretching modes of a mixture of monomeric $[\text{SnCl}_x(\text{H}_2\text{O})_{6-x}]^{4-x}$ species strongly decreases upon water addition, while the intensity of the line centered around 342 cm^{-1} increases. All these features evidence a change of tin halide speciation.

Quantitative evaluations of the observed transformations are presented in Figure 5 with the results of the first coordination shell by EXAFS fitting (Figure 5a) and tin halide speciation deduced from the areas of deconvoluted Raman lines corresponding to $x = 5, 4$, and 3 (Figure 5b). The EXAFS coordination numbers evolve from 4.6 ($t = 0$ min) to 3.9 ($t = 10$ min) for chlorine ligands and from 1.4 ($t = 0$ min) to 2.4 ($t = 10$ min) for coordinated oxygen atoms. Simultaneously, the proportion of $[\text{SnCl}_3(\text{H}_2\text{O})_3]^+$ species increases, the propor-

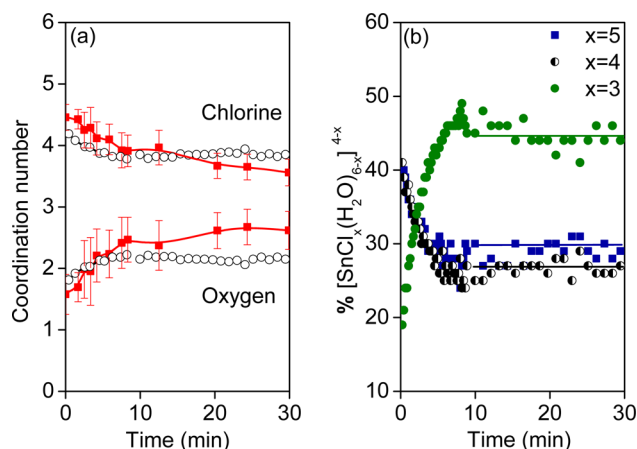


Figure 5. (a) Evolution of the coordination numbers N_{Cl} and N_{O} determined by (red ■) EXAFS fittings and (○) Raman deconvolution during the first 30 min of reaction. The error bars for the EXAFS coordination numbers are reported. (b) Compositional fractions of Sn-based species determined by deconvolution of the Raman spectra recorded during the first 30 min of reaction.

tions of both $[\text{SnCl}_5(\text{H}_2\text{O})]^-$ and $[\text{SnCl}_4(\text{H}_2\text{O})_2]$ species decrease with almost the same rate, which is 2 times slower than the formation rate of $[\text{SnCl}_3(\text{H}_2\text{O})_3]^+$. At the end of the water addition, the abundance of the species with $x = 3$ reaches about 45%, whereas those of the halide species with $x = 4$ and 5 are almost equivalent with about 25–30%. The Raman speciation of halide $[\text{SnCl}_x(\text{H}_2\text{O})_{6-x}]^{4-x}$ monomeric species can be used for calculating the average chlorine coordination numbers around Sn. These values are also compared with the values determined by EXAFS (Figure 5a). The close agreement between chlorine coordination numbers obtained by both techniques is well within the error bar for EXAFS fitted coordination numbers. Furthermore, during RT aging, the coordination numbers of oxygen atoms (deduced by Raman and assuming that N_{O} are only related to the presence of $[\text{SnCl}_x(\text{H}_2\text{O})_{6-x}]^{4-x}$ species) remain constant, whereas an increasing trend is verified for oxygen coordination numbers determined from EXAFS. The deviation of both N_{O} values is due to the formation of tin oxo species, like SnO_2 nanoparticles, which is neglected in the speciation from Raman data. It is noteworthy that during water addition the observed decrease of the distance between Sn and O from 2.11 to 2.08 Å (Table 1, Supporting Information), whereas the Sn–Cl distance remains invariant and equal to 2.38 Å and is well in line with the formation of SnO_2 for which the average Sn–O distance at 2.06 Å³⁹ is shorter than the Sn–O distance found in tin halide aquo complexes.⁴² Thus, results of both spectroscopic techniques are interpreted as the consumption of $[\text{SnCl}_5(\text{H}_2\text{O})]^-$ and $[\text{SnCl}_4(\text{H}_2\text{O})_2]$ complexes forming the more hydrated one, $[\text{SnCl}_3(\text{H}_2\text{O})_3]^+$, and oxo tin species (Sn–O–Sn). The latter are polynuclear species, as evidenced by the evolution of R_g determined by SAXS.

Actually, EXAFS spectra are satisfactorily analyzed with linear combinations (LC) of a representative EXAFS spectrum of the mixture of small polynuclear oxo species and $[\text{SnCl}_x(\text{H}_2\text{O})_{6-x}]^{4-x}$ complexes in solution, and the EXAFS spectrum of the SnO_2 nanoparticles extracted at the end of the synthesis. Such SnO_2 nanoparticles characterized by HRTEM and XRD, presented in Figure 6, have nanostructural features of the tridimensional tin oxo clusters (Figure 3) observed by

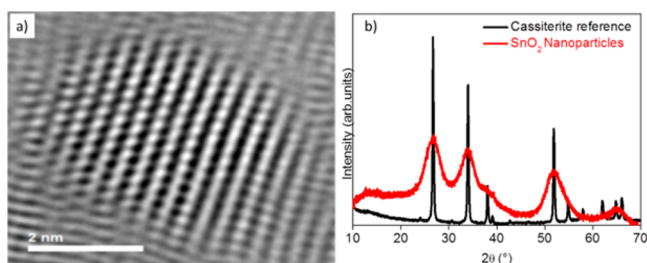


Figure 6. (a) HRTEM showing a SnO_2 single nanocrystal, (scale bar: 2 nm) recovered after 60 min of aging at 70°C and (b) XRD patterns of the recovered SnO_2 nanoparticles and of well crystalline cassiterite phase.

SAXS. The broad diffraction peaks evidence the formation of 3.5 nm average sized crystalline cassiterite structure as determined from Sherrer's equation.⁴⁸ According to SAXS, the pattern recorded between $t = 2.5$ min ($R_g = 2.6$ Å) and 4 min ($R_g = 3.5$ Å) is representative of the solution of mononuclear halide complexes and polynuclear species (dimers, trimers, and/or tetramers). The EXAFS spectrum corresponding to this reaction time is then used as a second component for the LC analysis to evaluate the percentage of SnO_2 nanoparticles formed during the period at RT and subsequent heating to 70°C . Typical LC fitting in k -space is presented in Figure S4 (Supporting Information). It is noteworthy that the FT moduli of the experimental EXAFS data displayed together with the FT of the LC EXAFS spectra in Figure S4 (Supporting Information) present in the 2–4 Å R -range a broad contribution of increasing intensity upon heating. This contribution is related to Sn–Sn contribution as deduced from the comparison with the FT moduli of the SnO_2 crystalline reference and of the SnO_2 nanoparticles extracted at the end of the synthesis.

Taking into account the speciation determined by EXAFS, which discriminates SnO_2 from the tin halide hydrated species, and the ones determined by Raman, which only focuses on tin halide hydrated species, we can renormalize the Raman speciation and present the tin speciation involving both spectroscopic data, as shown in Figure 7. In the first 4 min, where no SnO_2 clusters are observed, the $[\text{SnCl}_5(\text{H}_2\text{O})]^-$ and $[\text{SnCl}_4(\text{H}_2\text{O})_2]$ species are transformed into $[\text{SnCl}_3(\text{H}_2\text{O})_3]^+$.

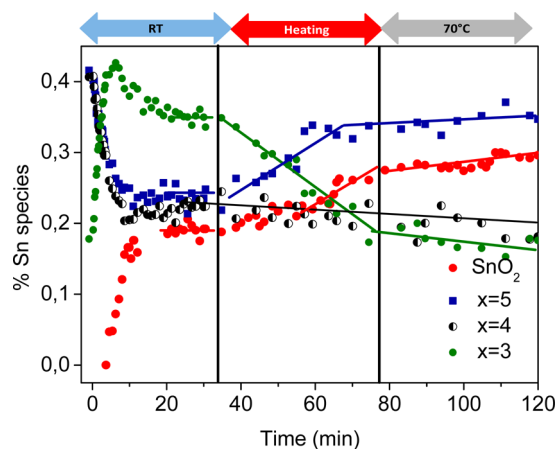


Figure 7. Compositional fractions of Sn based species determined by the deconvolution of the Raman data and fittings of EXAFS spectra recorded all along the reaction.

As already mentioned, the consumption rates of $[\text{SnCl}_5(\text{H}_2\text{O})]^-$ and $[\text{SnCl}_4(\text{H}_2\text{O})_2]$ species are equal and are half the rate of formation of $[\text{SnCl}_3(\text{H}_2\text{O})_3]^+$. The cationic species is then formed by the increase of hydration degree leading to the exchange of chlorine ligands belonging to the anionic and neutral tin halide complexes. At $t > 4$ min, the concentration of the $[\text{SnCl}_3(\text{H}_2\text{O})_3]^+$ reaches a plateau, whereas that of $[\text{SnCl}_5(\text{H}_2\text{O})]^-$ and $[\text{SnCl}_4(\text{H}_2\text{O})_2]$ keep decreasing and SnO_2 appear concomitantly. These findings are strong evidence that the halide species involved in the formation of SnO_2 are the anionic and neutral tin halide complexes. The neutral $[\text{SnCl}_4(\text{H}_2\text{O})_2]$ species, with no electrostatic repulsion, is expected to condense into polynuclear tin halide, oxo, or hydroxo species. The formation of such polynuclear tin halide species was not detected by Raman spectroscopy within the experimental time resolution used herein. During RT aging ($t > 10$ min), all the species reach a steady-state with no variation of their concentrations.

3.3. Effect of Heating and Aging at 70°C . Figure S5, (Supporting Information) presents time-selected SAXS spectra from the end of the RT aging ($t = 30$ min) through the heating stage ($30 < t < 70$ min) to the end of the isothermal aging at 70°C ($t = 120$ min). The main structural parameters, R_g and $I(0)$, extracted from the SAXS analysis are presented in Figure 8.

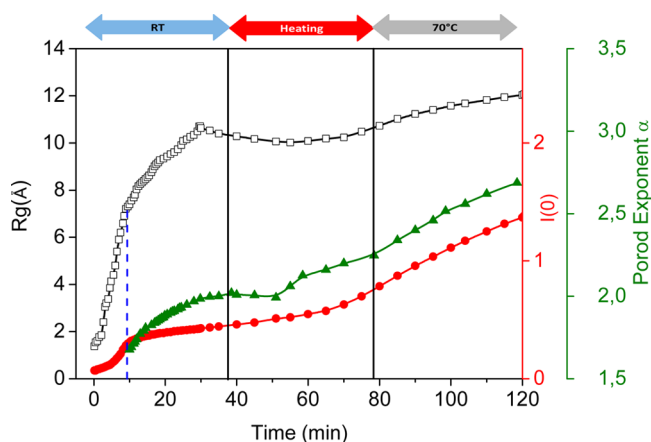


Figure 8. Time evolution of the main SAXS parameters, the radius of gyration R_g (black \square), $I(0)$ (red \bullet), and Porod exponent (green \blacktriangle).

Two different behaviors are observed: (1) during the heating, a slight decrease of R_g is observed, while $I(0)$ stays essentially constant; (2) during the isothermal stage, the plateau in the Guinier region is shifting toward smaller q -values indicating a secondary growth of the nanoparticles, $I(0)$ is also increasing and the Porod exponent varies from 2.2, at the beginning of the isothermal treatment, to 2.7 at the end. The unequivocal interpretation of such nanoscopic behaviors requires the complementary information about tin speciation coming from Raman and EXAFS.

The tin speciation during heating and aging is presented in Figure 7. An analysis procedure similar to the one described in section 3.2.2 was used. At the beginning of the heating stage, the profiles of concentrations of SnO_2 and neutral $[\text{SnCl}_4(\text{H}_2\text{O})_2]$ are quasi-constant, while the anionic and cationic complexes ones co-vary and essentially follow the same trend until the end of the reaction monitoring. Just before the beginning of the isothermal aging, a significant increase of the SnO_2 concentration is observed. It is interesting to note

that during the heating, the invariance of the quantities of tin atoms forming the SnO_2 nanocrystals is coinciding with the invariance of $I(0)$. That implies that the decrease of R_g can not be attributed to the dissolution of condensed SnO_2 species.

4. DISCUSSION

The different behaviors observed during water addition, RT aging, heating, and final aging at 70 °C are highlighted by the four regimes displayed by the $I(0)$ versus R_g^6 plot presented in Figure 9, namely, nucleation, growth, densification, and finally, secondary growth. These different regimes will be discussed in light of eq 2.

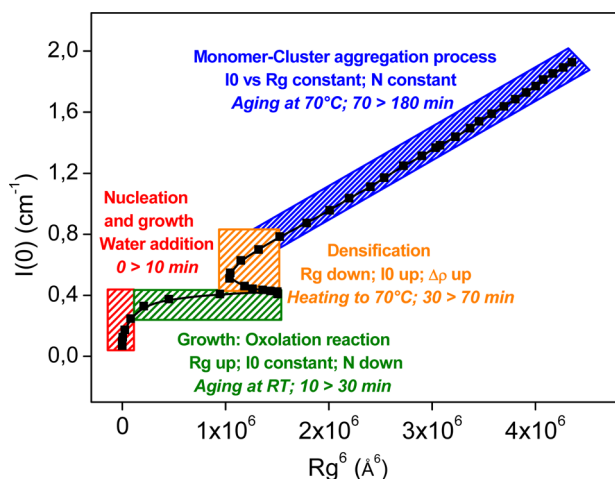
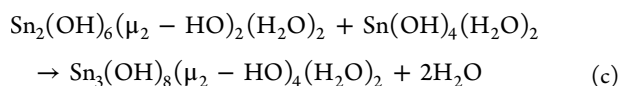
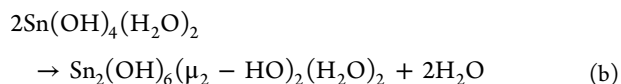
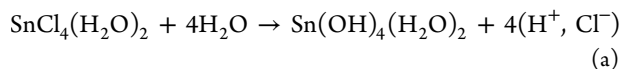


Figure 9. $I(0)$ versus R_g^6 plot showing the steps of the mechanisms of formation of SnO_2 nanoparticles: (red) nucleation, (green) growth, (orange) densification, and (blue) secondary growth.

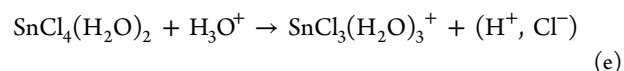
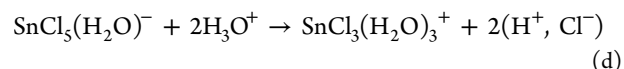
4.1. Nucleation Regime. During the first 5 min of water addition, a huge increase of $I(0)$ is observed, whereas R_g remains almost constant. This is the clear evidence of the increase of the number of scattering objects, as expected for the nucleation stage from a homogeneous solution. It is found that at the end of this stage ($t = 5$ min), the value of $R_g = 4$ Å is consistent with the formation of PNC composed of trinuclear linear edge-sharing octahedra (see schematics in Figure 3). It is important to note that such a prenucleus can be used as a building block of the cassiterite structure. The condensation into trinuclear linear PNC can be the result of the following reactions induced by the addition of water:



Although different tin halide monomeric complexes are evidenced in solution, due to the low nucleophilic character of water ligands, the condensation toward trinuclear edge sharing octahedral chain cannot occur directly from $[\text{SnCl}_x(\text{H}_2\text{O})_{6-x}]^{4-x}$; they occur from the neutral aquahydroxo tin precursor, $\text{Sn}(\text{OH})_4(\text{H}_2\text{O})_2$, formed from the full substitution of the Cl ligands. The ololation reactions (reactions

b and c) are the most likely between neutral aquahydroxo tin species due to the absence of electrostatic repulsion. It is worth noting that the amount of water consumed in the hydrolysis (reaction a) is equal to the total number of molecules released in the condensation reactions b and c. Thus, the addition of a large excess of water can limit the progress of the condensation reactions, displacing the equilibrium to the maintenance of the hydroxylated species.

Upon the addition of water, a strong release of hydronium ions occurs according to reaction a. Nevertheless, due to the dilution effect caused by the addition of water, no evidence of the pH decrease is observed for hydrolysis ratio below 60 (Supporting Information, Figure S1). Concomitant to the formation of PNC, Raman results evidence the increase of the hydration degree for tin halide complexes, according to the following reactions:



The strong acidity ($\text{pH} = 0.9\text{--}1.45$) together with the addition of a large excess of water stabilize the hydrolyzed species, decreasing the reactivity toward the condensation reaction. In this initial step, the nucleation rate's dominance over the growth rate is the necessary condition for the preparation of monodispersed nanocrystalline SnO_2 particles.

4.2. Growth Regime. This stage includes the end of the water addition ($5 < t < 10$ min) and the RT aging ($10 < t < 30$ min). $I(0)$ increases asymptotically to an almost constant regime, while R_g is following two striking linear regimes, first with an increase from 4 to 8 Å for $t < 10$ min and then from 8 to 11 Å for $t > 10$ min (Figure 3).

At the advanced stage ($t > 10$ min), a plateau-like feature is observed for the $I(0)$ versus R_g^6 plot, accompanied by a constant amount of tin atoms involved in SnO_2 nanoparticles (LC EXAFS analysis, Figure 7). It follows that N , the particle number density, is decreasing according to eq 2. This indicates the occurrence of the so-called cluster-cluster growth mechanism, where single chains of octahedra linked by edges are reacting with one another, forming double or triple chains structure; this corresponds to the secondary condensation by oxolation. The association of the chains by the corners occurs by oxolation reaction and directly leads to the growth of the crystalline cassiterite SnO_2 nanoparticles, as schematized in Figure 3. This crystalline structure is confirmed by the X-ray diffraction and by the HRTEM picture of the nanoparticles recovered at the end of the aging at 70 °C (Figure 6). Their 3.5 nm crystallite size is slightly larger than the average equivalent spherical size of the nanoparticles $D = 2.85$ nm determined by SAXS at the end of the RT aging ($D = 2R_g(5/3)^{1/2}$ with $R_g = 1.1$ nm).⁴¹

At the early growth stage ($5 < t < 10$ min), a transient regime is observed with an increase of condensed SnO_2 species and a concomitant decrease of mononuclear tin halide complexes in solution, as evidenced by the EXAFS speciation (Figure 7), while $I(0)$ and R_g simultaneously increase. This behavior indicates that tin oxo cluster growth occurs by the addition of monomeric species to PNC, which corresponds to a monomer-cluster aggregation mechanism. It is noteworthy that the onset of growth of SnO_2 nanoparticles coincides with the significant change in the pH evolution (Supporting Information, Figure

S1). Despite that water is still added (hydrolysis ratio increasing from 60 to 105), the pH decreases abruptly from 1.4 to 1.2. Then, the pH slope changes upon RT aging but still decreases from 1.2 to 1.0. Such pH modifications are additional evidence that a supplementary release of hydronium ions occurs at this stage, resulting from the aforementioned oxolation reactions at both growth stages.

4.3. Densification Regime. Upon heating of the suspension, an upturn of the curve $I(0)$ as a function of R_g^6 is observed. $I(0)$ is increasing, while R_g is decreasing, and the amount of tin atoms involved in SnO_2 nanoparticles is invariant (LC EXAFS analysis Figure 7). It follows that the electron density contrast ($\rho_p - \rho_s$), according to eq 2, is increasing, demonstrating the densification of the nanoparticles. The covariation of $[\text{SnCl}_3(\text{H}_2\text{O})_3]^+$ and $[\text{SnCl}_5(\text{H}_2\text{O})]^-$ (Figure 7) interpreted as the reverse reaction (reaction d), indicates a displacement of the equilibrium. We assume that the shift of reaction d toward the formation of $[\text{SnCl}_5(\text{H}_2\text{O})]^-$ is due to the release of chlorine ions from condensed SnO_2 nanoparticles. We propose that such a release is the result of intrabuilding blocks rearrangement caused by the reaction between terminal Cl and OH ligands (Sn–Cl and Sn–OH) leading to Sn–O–Sn bridges and thus to the densification. The crystallization of SnO_2 nanoparticles probably occurs at this stage.

4.4. Secondary Growth. This regime is characterized by a linear behavior of the $I(0)$ as a function of R_g^6 plot throughout the isothermal process at 70 °C. This implies a constant particle number N and electron density contrast ($\rho_p - \rho_s$) during the secondary growth process. This behavior is evidence that the secondary growth proceeds through the addition of mononuclear tin species to the surface of the growing nanoparticles, following once more the monomer–cluster–aggregation mechanism. This proposition is in agreement with the covariation of tin atom observed in Figure 7 for dissolved species (decreasing trend) and for SnO_2 nanoparticles (increasing trend). The consumption of monomers goes along with the change of the Porod region of the SAXS curves toward higher slopes which can also be interpreted as an evolution toward dense spherical 3D nanoparticles. The final SAXS pattern could be fitted with a sphere form factor function and a log-normal distribution. We obtain a final SnO_2 nanoparticle size of 2.5 nm and a size distribution of 35%. This is in good agreement with the diameter of the particles determined by HRTEM (2 and 3 nm) and with XRD results (Figure 6).

5. CONCLUSIONS

The mechanisms of hydrolysis/nucleation and condensation/growth of $\text{SnCl}_4 \cdot 5\text{H}_2\text{O}$ precursors in acid ethanol solution, induced by RT water addition, and subsequently followed by heating stage to 70 °C, leading to the formation of SnO_2 nanocrystals, have been unraveled by a combination of in situ Sn K-edge quick-EXAFS and Raman spectroscopies coupled to time-resolved SAXS measurements.

The Raman, EXAFS, and SAXS analysis of the initial precursor solution unequivocally evidence the presence of a mixture of tin chloride monomeric complexes $[\text{SnCl}_x(\text{H}_2\text{O})_{6-x}]^{4-x}$ composed of 41% $[\text{SnCl}_5(\text{H}_2\text{O})]^-$, 41% $[\text{SnCl}_4(\text{H}_2\text{O})_2]$, and 18% $[\text{SnCl}_3(\text{H}_2\text{O})_3]^+$.

We demonstrate that the formation of SnO_2 nanocrystals is composed of the following stages:

1. In the very early period of water addition (<5 min), until the nucleation rate reaches $[\text{H}_2\text{O}]/[\text{Sn}] = 60$, it dominates the growth rate, leading to the increase of the number of prenuclei. An average radius of gyration of 4 Å indicates that the prenuclei exist as linear trimers formed from oxolation reaction between monomeric aquahydroxo tin species.

2. A monomer tin oxo cluster aggregation mechanism is evidenced by the decrease of mononuclear tin complexes in solution and the concomitant increase of the size of the condensed SnO_2 species during the later stage of water addition, corresponding to $60 < [\text{H}_2\text{O}]/[\text{Sn}] < 105$.

3. A cluster–cluster growth mechanism involving the oxolation reaction between single chains of edge linked octahedra, forming double or triple chain structures, is observed during aging at room temperature. This interchain association, through octahedra corners, leads to the direct growth of the SnO_2 nanoparticles.

4. A densification of the SnO_2 nanoparticles, caused by the formation of Sn–O–Sn bridges and due to the reaction between terminal Cl and OH ligands (Sn–Cl and Sn–OH), is ascertained during the solution heating from RT to 70 °C.

5. A secondary growth regime is observed during the isothermal aging at 70 °C, which proceeds through the addition of mononuclear tin species to the surface of the growing nanoparticles, following the monomer–cluster–aggregation mechanism.

These five time-defined stages can be used as a versatile way to control the growth processes in order to fine-tune the size of SnO_2 nanocrystalline particles.

■ ASSOCIATED CONTENT

Supporting Information

Time evolution of the hydrolysis ratio, pH, and temperature during the in situ SAXS and Raman/EXAFS experiments; schematics of the experimental setups used for the SAXS and Raman/EXAFS in situ measurements; description of the EXAFS data analysis; example of Raman peak fitting procedure; typical EXAFS linear combinations fitting for the solutions; and time-selected SAXS spectra from the end of the RT aging through the heating stage to the end of the isothermal aging at 70 °C. This material is available free of charge via the Internet at <http://pubs.acs.org>.

■ AUTHOR INFORMATION

Corresponding Authors

*E-mail: florian.meneau@lnls.br.

*E-mail: caetano@iq.unesp.br.

Author Contributions

The manuscript was written through contributions of all authors.

Notes

The authors declare no competing financial interest.

■ ACKNOWLEDGMENTS

The authors wish to thank the SOLEIL synchrotron facility for providing beamtime at the SAMBA and SWING beamlines and Dr. S. Blanchandin for her assistance in the chemistry laboratory. The authors also would like to thank the Electron Microscopy Laboratory (LME) of the Brazilian Nanotechnology National Laboratory (LNNano) for the use of their HRTEM facility. This work was also partially supported by the National Council for Scientific and Technological Development

(CNPq) of Brazil, the Foundation for Research Support of the State of São Paulo (FAPESP), and the CAPES/COFECUB and CNRS/FAPESP cooperation programs.

■ REFERENCES

- (1) Wang, C.; Lu, B.; Zuo, J.; Zhang, S.; Tan, S.; Suzuki, M.; Chase, W. T. *Nanostruct. Mater.* **1995**, *5*, 489.
- (2) Hammer, P.; Rizzato, A. P.; Pulcinelli, S. H.; Santilli, C. V. *J. Electron Spectrosc. Relat. Phenom.* **2007**, *156*, 128.
- (3) Santos, L. R. B.; Larbot, A.; Persin, M.; Santilli, C. V.; Pulcinelli, S. H. *J. Sep. Purif. Technol.* **2001**, *22&23*, 17.
- (4) Kida, T.; Doi, T.; Shimano, K. *Chem. Mater.* **2010**, *22*, 2662.
- (5) Zhou, Z. Y.; Tian, N.; Li, J. T.; Broadwell, I.; Sun, S. G. *Chem. Soc. Rev.* **2011**, *40*.
- (6) Ellmer, K. *Nat. Photonics* **2012**, *6*, 808.
- (7) Goebbert, C.; Nonninger, R.; Aegerter, M. A. *Thin Solid Films* **1999**, *351*, 79.
- (8) Sanchez, C.; Rozes, L.; Ribot, F.; Laberty-Robert, C.; Grosso, D.; Sassoye, C.; Boissiere, C.; Nicole, L. C. R. *Chim.* **2010**, *13*, 3.
- (9) Hampden-Smith, M. J.; Wark, T. A.; Brinker, C. J. *Coord. Chem. Rev.* **1992**, *112*, 81.
- (10) Ribot, F.; Martinez-Ferrero, E.; Boubekur, K.; Hendrickx, P. M. S.; Martins, J. C.; Van Lokeren, L.; Willem, R.; Biesemans, M. *Inorg. Chem.* **2008**, *47*, 5831.
- (11) Ha, H.-W.; Kim, K.; de Borniol, M.; Toupance, T. *J. Solid State Chem.* **2006**, *179*, 702.
- (12) Briois, V.; Belin, S.; Zucolotto Chalaça, M.; Santos, R. H. A.; Santilli, C. V.; Pulcinelli, S. H. *Chem. Mater.* **2004**, *16*, 3885.
- (13) Pinna, N.; Neri, G.; Antonietti, M.; Niederberger, M. *Angew. Chem., Int. Ed.* **2004**, *43*, 4345.
- (14) Wang, H.; Rogach, A. L. *Chem. Mater.* **2014**, *26*, 123.
- (15) Jensen, K. M. Ø.; Christensen, M.; Juhas, P.; Tyrsted, C.; Bøjesen, E. D.; Lock, N.; Billinge, S. J. L.; Iversen, B. B. *J. Am. Chem. Soc.* **2012**, *134*, 6785.
- (16) Zhou, X.; Zhou, T.; Hu, J.; Li, J. *CrystEngComm* **2012**, *14*, 5627.
- (17) LaMer, V. K.; Dinegar, R. H. *J. Am. Chem. Soc.* **1950**, *72*, 4847.
- (18) LaMer, V. K. *Ind. Eng. Chem.* **1952**, *44*, 1270.
- (19) Finney, E. E.; Finke, R. G. *J. Colloid Interface Sci.* **2008**, *317*, 351.
- (20) Gebauer, D.; Cölfen, H. *Nano Today* **2011**, *6*, 564.
- (21) Polte, J.; Tuae, X.; Wuithschick, M.; Fischer, A.; Thuenemann, A. F.; Rademann, K.; Kraehnert, R.; Emmerling, F. *ACS Nano* **2012**, *6*, 5791.
- (22) Ustarroz, J.; Hammons, J. A.; Altantzis, T.; Hubin, A.; Bals, S.; Terryn, H. *J. Am. Chem. Soc.* **2013**, *135*, 11550.
- (23) Gebauer, D.; Kellermeier, M.; Gale, J. D.; Bergstrom, L.; Colfen, H. *Chem. Soc. Rev.* **2014**, *43*, 2348.
- (24) Wang, F.; Richards, V. N.; Shields, S. H.; Buhro, W. E. *Chem. Mater.* **2014**, *26*, 5.
- (25) Baumgartner, J.; Dey, A.; Bomans, P. H. H.; Le Coadou, C.; Fratzl, P.; Sommerdijk, N. A. J. M.; Faivre, D. *Nat. Mater.* **2013**, *12*, 310.
- (26) Peng, Z. A.; Peng, X. *J. Am. Chem. Soc.* **2002**, *124*, 3343.
- (27) Soloviev, V. N.; Eichhofer, A.; Fenske, D.; Banin, U. *J. Am. Chem. Soc.* **2001**, *123*, 2354.
- (28) Ran, S.; Fang, D.; Sics, I.; Toki, S.; Hsiao, B. S.; Chu, B. *Rev. Sci. Instrum.* **2003**, *74*, 3087.
- (29) Briois, V.; Lützenkirchen-Hecht, D.; Villain, F.; Fonda, E.; Belin, S.; Griesbeck, B.; Frahm, R. *J. Phys. Chem. A* **2005**, *109*, 320.
- (30) Kongmark, C.; Martis, V.; Rubbens, A.; Pirovano, C.; Löfberg, A.; Sankar, G.; Bordes-Richard, E.; Vannier, R.-N.; Van Beek, W. *Chem. Commun.* **2009**, 4850.
- (31) Iglesias-Juez, A.; Beale, A. M.; Maaijen, K.; Chien Weng, T.; Glatzel, P.; Weyckhuysen, B. M. *J. Catal.* **2010**, *276*, 268.
- (32) Caetano, B. L.; Santilli, C. V.; Meneau, F.; Briois, V.; Pulcinelli, S. H. *J. Phys. Chem. C* **2011**, *115*, 4404.
- (33) Fouilloux, F.; Taché, O.; Spalla, O.; Thill, A. *Langmuir* **2011**, *27*, 12304.
- (34) Chao, Y.; Horner, O.; Vallée, P.; Meneau, F.; Alos-Ramos, O.; Hui, F.; Turmine, M.; Perrot, H.; Lédion, J. *Langmuir* **2014**, *30*, 3303.
- (35) Briois, V.; Fonda, E.; Belin, S.; Barthe, L.; La Fontaine, C.; Langlois, F.; Ribbens, M.; Villain, F. *UVX 2010* **2011**, 41.
- (36) Fonda, E.; Rochet, A.; Ribbens, M.; Barthe, L.; Belin, S.; Briois, V. *J. Synchrotron Radiat.* **2012**, *19*, 417.
- (37) Ravel, B.; Newville, M. *J. Synchrotron Radiat.* **2005**, *12*, 537.
- (38) Newville, M. *J. Synchrotron Radiat.* **2001**, *8*, 322.
- (39) Baou, W. H. *Acta Crystallogr.* **1956**, *9*, 515.
- (40) Miller, G. A.; Schlemper, E. O. *Inorg. Chim. Acta* **1978**, *30*, 131.
- (41) Craievich, A. In *Handbook of Sol-Gel Science and Technology*, Sakka, S., Ed.; Kluwer Academic Publishers: Boston, 2005, *2*, p 161.
- (42) Shihada, A.-F.; Abushamleh, A. S.; Weller, F. *Z. Anorg. Allg. Chem.* **2004**, *630*, 841.
- (43) Semenov, S. N.; Maltsev, E. Y.; Timokhin, I. G.; Drozdov, A. A.; Troyanov, S. I. *Mendeleev Commun.* **2005**, *15*, 205.
- (44) Taylor, M. J.; Coddington, J. M. *Polyhedron* **1992**, *11*, 1531.
- (45) Placzek, G. In *Handbuch der Radiologie*, Marx, E., Ed.; Akademische Verlagsgesellschaft: Leipzig, 1934, p 209.
- (46) Guinier, A.; Fournet, G. *Small-Angle Scattering of X-rays*; Wiley: New York, 1955.
- (47) Li, X.; Shew, C.-Y.; He, L.; Meilleur, F.; Myles, D. A. A.; Liu, E.; Zhang, Y.; Smith, G. S.; Herwig, K. W.; Pynn, R.; Chen, W.-R. *J. Appl. Crystallogr.* **2011**, *44*, 545.
- (48) Scherrer, P. *Göttinger Nachrichten Math. Phys.* **1918**, *2*, 98.